Lab on a Chip
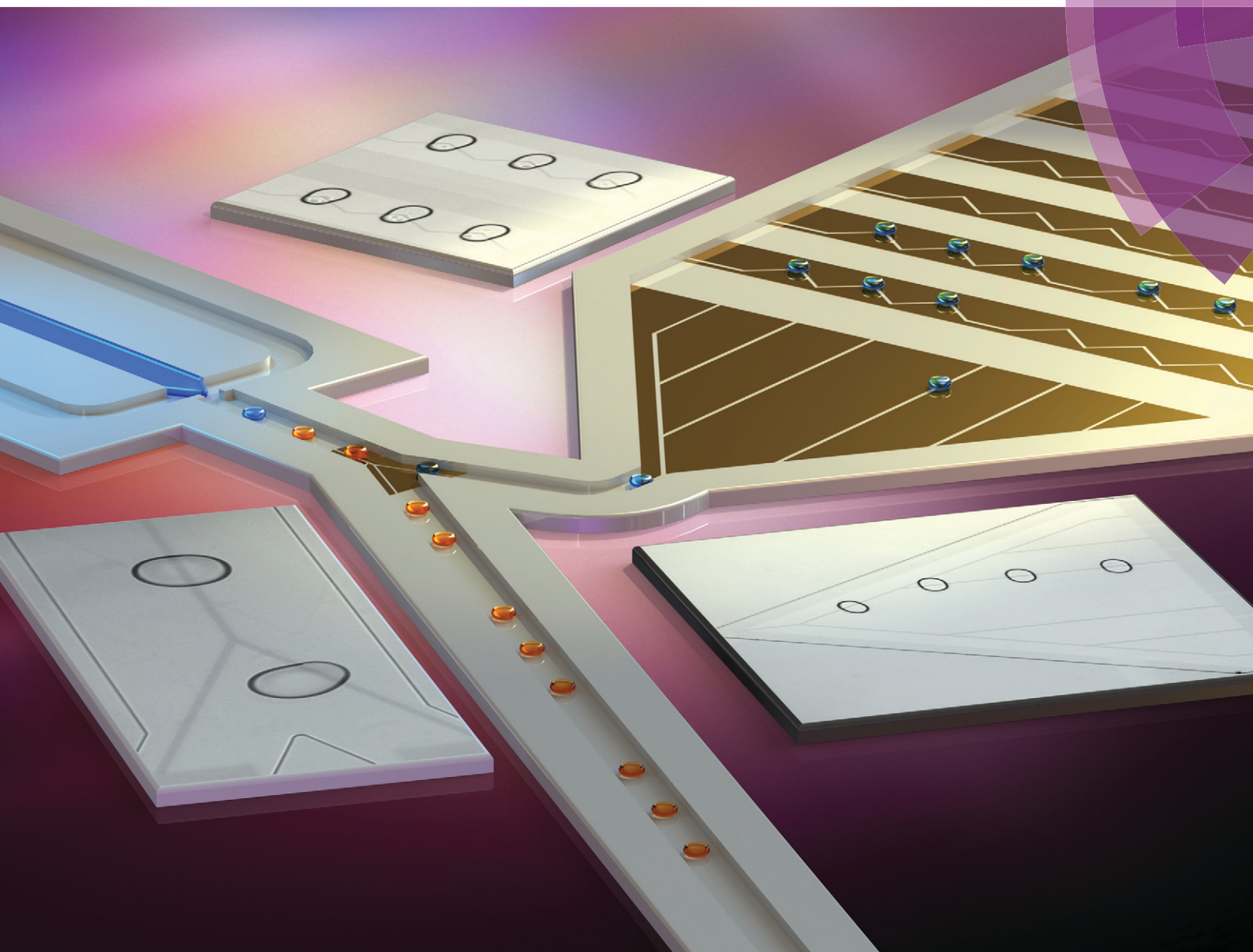
Miniaturisation for chemistry, physics, biology, materials science and bioengineering

www.rsc.org/loc

ROYAL SOCIETY
OF CHEMISTRY

PAPER
Riëlle de Ruiter *et al.*
Electrostatic potential wells for on-demand drop manipulation
in microchannels

Electrostatic potential wells for on-demand drop manipulation in microchannels†

Riëlle de Ruiter,* Arjen M. Pit, Vitor Martins de Oliveira, Michèl H. G. Duits, Dirk van den Ende and Frieder Mugele

Precise control and manipulation of individual drops are crucial in many lab-on-a-chip applications. We present a novel hybrid concept for channel-based discrete microfluidics with integrated electrowetting functionality by incorporating co-planar electrodes (separated by a narrow gap) in one of the microchannel walls. By combining the high throughput of channel-based microfluidics with the individual drop control achieved using electrical actuation, we acquire the strengths of both worlds. The tunable strength of the electrostatic forces enables a wide range of drop manipulations, such as on-demand trapping and release, guiding, and sorting of drops in the microchannel. In each of these scenarios, the retaining electrostatic force competes with the hydrodynamic drag force. The conditions for trapping can be predicted using a simple model that balances these forces.

Introduction

In various fields in (cell) biology and chemistry, microfluidic drops are currently used as microreactors of picoliter to nanoliter volume with an isolated and controlled content.[1,2] By injecting the analyte fluid into T-junctions[3,4] or flow focusing devices,[5] or using microchannel step emulsification,[6–8] monodispersed liquid drops can be generated up to kHz frequencies in channel-based discrete microfluidics. However, applications such as high-throughput screening of cells and analysis of chemical reactions require in addition high-speed manipulation and individual control over specific drops.

In flow or pressure driven microfluidics, drops are mostly manipulated passively *via* topological modification of the channels, *e.g.* by using variations in the channel dimensions to modify the hydrodynamic resistance of different paths or capillary valves to modify the pressure required for drop transport. Several drop manipulations have been demonstrated, such as transport, trapping, sorting, merging, and splitting.[1,9–11] An illustrative example is the trapping of drops in storage wells connected to the main channel, making use of a combination of capillary

Physics of Complex Fluids and MESA+ Institute for Nanotechnology, University of Twente, P.O. Box 217, 7500 AE Enschede, The Netherlands.
E-mail: r.deruiter-1@utwente.nl

† Electronic supplementary information (ESI) available: Details of the derivation of the analytical expression and the numerical calculations concerning the hydrodynamic drag force. Movie S1 of a drop interacting with co-planar electrodes for $U = 0$, $0 < U < U_c$, and $U \geq U_c$. Movie S2 of alternate sorting of drops at 23 drops per second. Movie S3 of the selection of a single drop. See DOI: 10.1039/c3lc51121a

forces and differences in hydrodynamic resistance. An alternative flow path is present for the continuous phase in the form of bypass channels when the wells are occupied.[12,13] On the other hand, drops can also be trapped at specific locations in the main channel itself. Small holes have been introduced in the top wall of a wide and thin microchannel to function as anchors. Confined drops that are passing by expand into the hole to decrease their surface area and interfacial energy, generating an anchoring force that can hold the drop against the drag force of the surrounding flow.[14,15] The merging of subsequent drops has been achieved for example by widening the channel[16] or capturing drops in between rows of pillars,[17] and splitting is accomplished in T-junctions or by introducing isolated obstacles in the flow.[18–20] Since these passive manipulations are in general non-selective and not (easily) tunable, precise control over individual drops is limited. For example, a drop trapped in a storage well or by a small geometric defect in the microchannel wall cannot be easily released by changing the trapping force. To remove the drop from the trap, a change in the direction or magnitude of the flow is required.[12–15] Another possible disadvantage is that if arrays of drops are trapped, they will all be released simultaneously. A combination of active methods, *e.g.* laser forcing[21] or dielectrophoresis,[22] is necessary to release single drops.

Precise control over individual drops can be achieved *via* electrowetting-based digital microfluidics (DMF), in which units of nanoliter to microliter volume are actuated using a series of adjacent electrodes.[23–27] The same types of drop manipulation as described above are then performed *via* switching of individually addressable electrodes that change the local wettability. As the electrodes provide the actuation, no driving flow is used. Devices are either based on a parallel plate set-up,

in which drops are sandwiched between a substrate with insulated actuation electrodes and a substrate with ground electrodes, or on co-planar designs, where both the actuation and ground electrodes are patterned on one substrate. Although high actuation speeds can be achieved in DMF, the throughput is always lower than in channel-based microfluidics. In addition, higher throughputs require extensive programming of a large number of electrodes.

Here, we combine the high throughput and low sample volumes used in channel-based microfluidics and the individual drop control achieved using electrical actuation by incorporating insulator-covered electrodes in the walls of microchannels. The isolation of the electrodes from the aqueous drops offers clear advantages over designs in which there is direct contact between electrodes and fluid,[28,29] as it prevents electrochemical reactions that could be detrimental to various (*e.g.* biological) samples. Electrodes can be positioned at various locations along the channel in several configurations to perform different drop manipulations, thereby fully integrating the two techniques spatially. This approach differs from a previous hybrid design where a co-planar digital microfluidics unit was placed on the front end of a microchannel-based continuous flow system.[30] Here, DMF was used to pre-process liquid drops, after which a small fraction was loaded into the channel for single phase chemical separations. The voltages required for the electrical actuation of drops depend on the thickness of the dielectric layer, but they are generally much lower than the kilovolts used in dielectrophoretic (DEP) actuation, where polarizable drops are manipulated with non-uniform electric fields.[22,31–33] In addition, electrical actuation offers a more direct and local control, allowing for drop trapping above the electrodes inside the main microchannel.

In previous work by our group, the combination of microfluidics and electrowetting (EW) was used to control the size and frequency of drop formation.[34,35] We now use a different approach; instead of contact angle reduction, we exploit electrostatic potential wells to manipulate drops in a microchannel flow. Several operations can be implemented, such as on-demand trapping and release, which is crucial for the storage of drops that need to be analysed *in situ* for some time. To create a trapping site we use two co-planar electrodes[36] separated by a narrow gap. A co-planar design allows for easy fabrication of the microfluidic device, as the (PDMS) channels only need to be connected to a single insulator-covered substrate with both the actuation and ground electrodes. In more complex lab-on-a-chip devices, such co-planar electrodes can be combined with another functional unit in the second substrate. For example, drops with cells can be trapped in specific positions where ligands are patterned in the opposing channel wall, allowing for the analysis of excreted proteins using Surface Plasmon Resonance (SPR)[37] or other techniques.

When a confined conductive drop is positioned above both insulator-covered electrodes, a series of two parallel-plate capacitors is formed, which generates an electrical potential well that tends to keep the drop above the two electrodes. The associated attractive force is proportional to the square of the applied voltage, allowing for a tunable trapping strength.[38]

The equilibrium position of the drop (with respect to the trap) is governed by a force balance between the retaining and driving forces. The latter is the hydrodynamic drag force exerted by the continuous phase flow, which is adjustable *via* the flow rate. The trapping and driving forces are thus adjustable independently. In section I we discuss the principle and modelling of the electrostatic trap and compare the trapping and driving forces under various experimental conditions. The versatility of our approach for several applications in lab-on-a-chip devices is illustrated in section II. We demonstrate the guiding and sorting of drops, offering a simple alternative to sorting *via* dielectrophoresis[31,33] or surface acoustic waves.[39]

Materials and methods

The microchannels were fabricated from polydimethylsiloxane (PDMS, Sylgard 184) using standard soft lithography.[40] Fig. 1A gives an overview of the device, which consists of a (tapered) T-junction where aqueous drops are formed and a main channel containing the electrodes. The height of the device is 85 μm, and the width of the main channel is 2.5 mm. Due to the extreme aspect ratio the main channel can be considered as a Hele-Shaw cell.[41] The side inlets are used to control the oil flow rate in the main channel; this allows choosing the oil flow rates for drop formation and drop transport independently.

The bottom substrate is fabricated from indium tin oxide (ITO) coated glass substrates (PGO). Patterned electrodes are obtained *via* photolithography and etching in a solution of 18% HCl, creating gaps that are 10 or 15 μm wide. The substrate is spin coated with PDMS at 4000 rpm for 600 s to obtain an approximately 7 μm thick insulating layer that separates the aqueous drops from the electrode. While other insulating materials are generally preferable in EW, the use of PDMS was found to provide the most robust devices in terms of channel-to-substrate adhesion and leak-tightness. The PDMS is partly cured (at 75 °C for 20 min) and subsequently connected to the microchannels, while the electrodes are aligned in the main
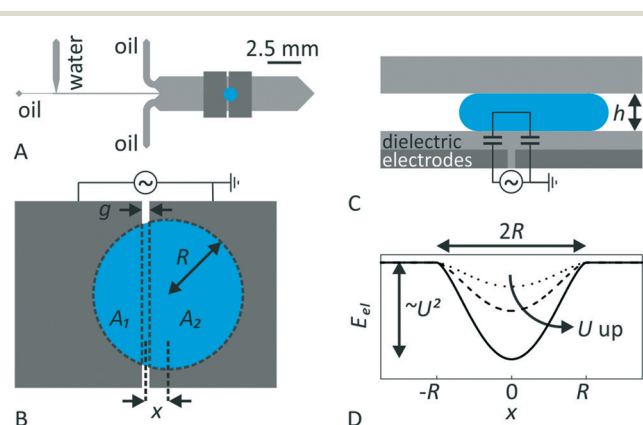

Fig. 1 Device geometry and generated electrostatic potential well. (A) Overview of one of the devices showing a drop formation unit and a main channel with trapping electrodes. (B) Top view and (C) side view of the co-planar electrode design. (D) Electrostatic potential well generated by the electrodes.

channel. Hereafter, the curing is completed. The properties of the dielectric layer are measured from the electrowetting response, *i.e.* the voltage-dependent contact angle $\cos(\theta) = \cos(\theta_Y) + \eta$ on a simultaneously fabricated evenly covered flat substrate. Here, θ_Y is the Young angle, and $\eta = \varepsilon_0\varepsilon_d U^2/(2d\sigma)$ is the electrowetting number,[23] where $\varepsilon_0\varepsilon_d$ is the dielectric permittivity of the substrate with thickness d, U is the applied root mean square (RMS) voltage, and σ is the interfacial tension of the oil/water interface. Using this method, the capacitance per area $c = \varepsilon_0\varepsilon_d/d$ of the dielectric layer is determined to be ~2.5 μF m^{-2}. The effective electrowetting number in the experiments is generally <1.

Paraffin oil (viscosity $\mu \approx 100$ mPa s) is used as the continuous phase, and the dispersed phase consists of de-ionized water (Millipore Synergy UV, 18.2 MΩ cm) with KCl added up to a conductivity of 3 mS cm^{-1} (~25 mM). The interfacial tension of the water/oil interface is 50 mN m^{-1}, and the advancing and receding water contact angles on PDMS are determined to be 148° and 138°, respectively. To study the influence of σ, a mixture of 50% (w/w) ethylene glycol and 50% (w/w) water is used. The interfacial tension is reduced to 33 mN m^{-1}, and the advancing and receding contact angles are now 148° and 132°.

Continuous oil flows are driven using syringe pumps. The dispersed phase is brought to the tapered T-junction by adjusting the water pressure. The required pressure depends on the applied oil flow rate and the hydraulic resistance of the channels. Drops are subsequently formed on demand by generating short air-pressure pulses using a pressure regulator (Parker Hannifin Corp.), a three-way solenoid valve (Takasago Electric Inc.), and a solid state relay (International Rectifier) which are controlled using home-made circuitry, a data acquisition card (National Instruments), and a custom-written MATLAB program. The air pressure can be regulated from about 1–100 kPa. Drops of different size ($R = 50$–250 μm) are generated by varying the duration Δt and magnitude ΔP of the pressure pulse. An alternating (AC) voltage (frequency: 1 kHz, RMS voltage: 0–350 V) is applied between the two separated electrodes in the main channel to generate electrostatic forces on the drops. The device is observed using an inverted microscope (TI-U, Nikon), and the behaviour of the generated drops is recorded using a high speed camera (FASTCAM SA5, Photron). Drop sizes are extracted using edge detection in MATLAB.

Results

I. Principles of on-demand trapping and release

A. Electrostatic potential wells. We first discuss the potential wells as generated by two co-planar electrodes separated by a gap. This case has already been described by 't Mannetje *et al.*[38] for spherical-cap shaped drops resting on an open surface. In our case, the drops are confined between the bottom and top walls of a microchannel, where the radii of the drops in the horizontal plane are larger than the height of the channel ($R > h$). Nevertheless, the underlying physical principles are the same for these two traps.

Briefly, when a confined drop of an electrically conductive liquid 'touches' (*i.e.* capacitively couples to) both electrodes,

an electrical circuit containing two parallel plate capacitors in series is formed (Fig. 1C). For the salt concentrations and AC frequencies considered in our experiments, the liquid can be considered as a perfect conductor (*i.e.* surface charges completely screen the electric field from the interior of the drop).[42] The capacitance between the drop and the electrodes is completely dominated by the area of the drop–substrate interface with negligible contributions from the contact line. Restricting our analysis to confined water drops with $R > h$, the contribution of oil intervening between the drop and the solid wall is reduced to a thin film that is negligible compared to the much thicker dielectric layers.[43] We note, however, that our device is also capable of trapping drops with $R > h$ – albeit with somewhat reduced trapping forces as compared to the analysis presented below.

The overall capacitance is $C(x) = C_1(x)C_2(x)/(C_1(x) + C_2(x))$, where the individual capacitances are given by $C_{1,2}(x) = (\varepsilon_0\varepsilon_d/d)A_{1,2}(x)$. Here, $A_{1,2}(x)$ is the area of the squeezed drop above the respective electrode. The areas depend on the position x of the center of mass of the drop (see Fig. 1B). Charging the capacitors by applying a voltage generates an electrostatic free-energy landscape $E_{el}(x) = -C(x)U^2/2 = -cAU^2 f(x)$, where $A = \pi R^2$ is the total contact area of the drop. The dimensionless function $f(x)$ can be derived from geometry and accounts for the variations in the areas (two examples are shown using the red curves in Fig. 2). The corresponding trapping force $F_{el}(x) = -dE_{el}(x)/dx$ has a maximum value $F_{el,max} = -acRU^2$. We thus find that the maximum trapping force scales with the capacitance per area, the radius of the (squeezed) drop, and the square of the voltage, with a proportionality constant a of order unity that depends on the electrode configuration. In this simplified analysis the voltage-dependent contact angle change and the resulting changes in the drop shape are neglected. Estimates show an increase in $F_{el,max}$ of maximum 20% for most experiments.

We now consider specific cases. For a gap between two (effectively) infinite electrodes (Fig. 2A), the electrostatic energy is minimal when the drop is centred above the gap. For a negligible gap width ($g \ll R$), the trapping force reaches a maximum $F_{el,max} = -0.58cRU^2$ at $x/R \approx 0.67$. In a microchannel with the gap oriented perpendicular to the flow direction, the hydrodynamic forces will tend to push the drop through the potential well, leading to a counteracting force in the downstream half of the potential and the possibility of drop trapping between $x/R = 0$ and $x/R \approx 0.67$. If the drag force exceeds the maximum value of the electrostatic force, the drop will pass the trap. In case the gap runs parallel to the flow direction in between two finite electrodes (Fig. 2B), the hydrodynamic forces will push the drop towards the edge of the electrodes. The areas of the drop above each electrode (always equal due to energy minimization) decrease as the drop is passing the trap. The electrostatic energy is now minimum if the drop is still completely in contact with the electrodes, and increases continuously afterwards. The trapping force reaches its maximum $F_{el,max} = -(1/4)cRU^2$ at $x/R = 0$, *i.e.* when the drop is halfway down the edge of the electrodes (note that this maximum force is 57% lower as compared to the perpendicular gap).
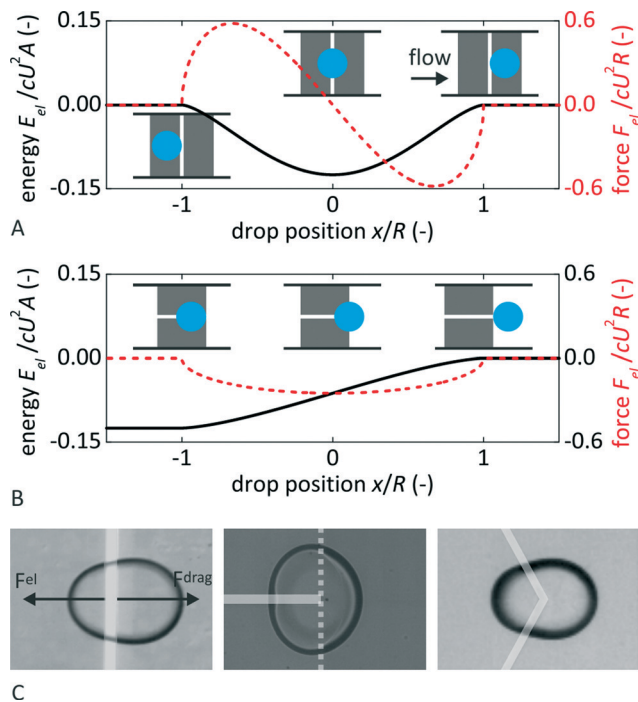
A

B

C

Fig. 2 Drop trapping in electrostatic potential wells. (A–B) The electrostatic contribution to the free energy of the system (black solid line) and the resulting electrostatic force (red dashed line) for two co-planar electrodes separated by a narrow gap ($g \to 0$) (A) perpendicular and (B) parallel to the direction of the flow. (C) Examples of drop trapping in various co-planar electrode designs: perpendicular gap, parallel gap, and V-shaped gap. The gaps between the electrodes are indicated in white.

Fig. 2C shows drops that are trapped using these two configurations (perpendicular (left) and parallel gaps (middle)) and a V-shaped gap (right). The choice of electrode configuration should be made in relation to the desired application. While the perpendicular gap yields the largest trapping force, the drops are free to move along the gap after trapping. In contrast, the parallel gap has a smaller trapping strength but has the benefits of keeping the drops on a predefined track in the microchannel and confining the trapped drop to a specific position. In addition, the inherent voltage-dependent elongation of the drop perpendicular to the gap (to be discussed in section II) is smaller in the parallel gap. The V-shaped gap directs the drop to the middle of the trap upon trapping. To facilitate the experiments and quantitative modelling of the forces acting on trapped drops, we chose the parallel gap for the present study.

B. Trapping experiments. To examine the trapping capability of our split-electrode configuration, we formed drops of a specific size ($R = 150$ μm) and recorded videos at several voltages (see Movie S1†). The extracted drop trajectories are shown in Fig. 3A. All drops have the same initial velocity of 0.3 mm s^{-1}, which is slightly lower than the average velocity of 0.8 mm s^{-1} of the continuous phase. As expected, when no voltage is applied, the drop traverses the microchannel without changing its velocity. At low voltages, the drop decelerates as soon as it starts crossing the edge of the electrodes, *i.e.* at $x/R = -1$. However, as long as the drag force exceeds the maximum electrostatic force, the drop passes

the trap and accelerates back to its initial velocity. Trapping of the drop only occurs when the RMS voltage exceeds a critical value U_c. The drop is slowed down until a zero velocity is attained at a voltage-dependent trapping position $x/R < 0$ and can subsequently be released on demand by switching off the voltage. A further increase in the voltage shifts the trapping position upstream (results not shown).

To investigate how this critical voltage U_c depends on the size of the drops, we performed systematic experiments that involved varying the drop size ($R = 50$–250 μm) and the applied voltage ($U = 100$–350 V) independently and recording the fate (*i.e.* passing or trapping) of each drop. The flow rate of the continuous phase in the test section with the trap was held constant. The results shown in Fig. 4A clearly indicate that U_c increases with R. Since the electrostatic force is proportional to the drop radius, it is implied that the hydrodynamic 'release force' increases more strongly with R. This also means that the trap is size-selective; for each given voltage we find a critical drop radius R_c above which the drop cannot be trapped anymore. Extending the systematic measurements to a second
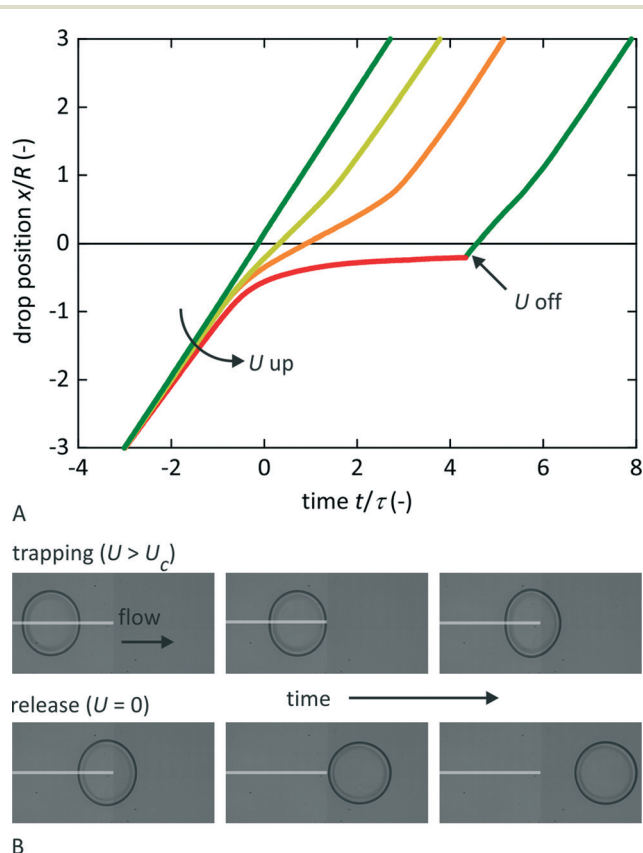

A

B

Fig. 3 Drop trajectories during trapping and release. (A) Drop trajectories upon passing the co-planar electrode configuration. The time is rescaled with τ, the characteristic time in which the undisturbed drop traverses its radius. For $U = 0$, (green) the drop has a constant velocity, for $0 < U < U_c$ (100 V (yellow) and 140 V (orange)), the drop is slowed down at the trap, and for $U \geq U_c$ (180 V (red)), the drop is ultimately trapped. Trapped drops can be released on demand by switching off the voltage. (B) Image sequences showing on demand drop trapping and release. The gaps between the electrodes are indicated in white.

flow rate, we found that the critical voltage increases with the continuous phase velocity u. Next, drops of a fixed size were formed at several flow rates to explore this dependence in more detail. As shown in Fig. 4B, a linear relationship is found between the square of the critical voltage (and thus the maximum electrostatic force) and the continuous phase velocity. Repeating these experiments at a different oil/water interfacial tension (by using an ethylene glycol–water mixture instead of water), we found that the critical voltage does not depend on σ at small applied voltages. At larger voltages, small deviations from this behavior are observed. Low interfacial tension drops are more deformed (see inset) and have a larger voltage-dependent contact angle reduction during guiding and trapping, resulting in a larger maximum trapping force.

C. Quantitative analysis. To explain the dependence of the critical voltage on drop size and flow rate (but not on interfacial tension), we consider the balance between the maximum electrostatic trapping force and the hydrodynamic driving force on the drop in a quantitative way. More accurate values for the trapping force are obtained by taking into account the finite gap width between the electrodes. A gap width g introduces a correction factor of $(1 - g/2R)$ to the trapping force, which is >0.85 for gaps that are 10–15 μm wide and drop radii that are larger than 50 μm. Edge detection yields the maximum drop radius, which is converted into the contact radius by taking into account the voltage-dependent contact angle (yielding <20% corrections). Drop deformations during trapping are neglected. The hydrodynamic drag force exerted by the outer flow is obtained from the Stokes equation. When $h \ll R$ the microchannel can be modelled as a Hele-Shaw cell, where the problem is reduced to a 2D flow by averaging the velocity field over the height of the channel. The total drag force on the drop contains two contributions: the pressure difference along the drop and the

viscous shear stresses in the surrounding fluid. Scaling arguments yield expressions for the pressure drag and viscous drag as $F_p \propto \mu u R^2/h$ and $F_\mu \propto \mu u R$, respectively.[15] This indicates that the pressure drag is larger than the viscous drag by an order of $R/h > 1$. An analytical calculation of the drag force on a cylinder with no-slip boundary condition in an infinitely wide channel yields $F_{\mathrm{drag}} = (24\pi\mu u R^2/h)(1 + 2K_1(q)/(qK_0(q)))$, where K_0 and K_1 are modified Bessel functions of the second kind and $q = 2\sqrt{3}R/h$ (see ESI†). These results agree well with the ones obtained by Lee and Fung.[44] For $R \gg h$, this expression is reduced to $F_{\mathrm{drag}} = 24\pi\mu u R^2/h$, which confirms the dominance of the pressure drag in the limit of large drops, while for $R \sim h$ the viscous drag needs to be considered as well (see Fig. S1†). It should be noted that the drag force is underestimated when the drop size becomes of the order of the finite channel width. The flow velocity is increased as the drop blocks a significant fraction of the channel width. In addition, the no-slip boundary condition at the confining side walls has to be taken into account. Thus, the width of the microchannel is the third length scale in the equation aside from the drop radius and the channel height. The numerically calculated curves in Fig. S1B† clearly demonstrate that the pressure difference along the drop shows a drastic increase as the drop radius approaches the width of the channel (i.e. $2R/h \approx W/h$), resulting in a diverging drag force. More details about these calculations can be found in the ESI† and in the study of Vanapalli et al.[45] Since $R/h < 3$ in the current experiments, the analytical expression is used to determine the drag force.

Plotting the drag force against the maximum trapping force in Fig. 5, we find a sharp transition from passing to trapping as soon as the maximum trapping force exceeds the hydrodynamic drag. The experimental data for several flow rates and interfacial tensions follow the same curve,
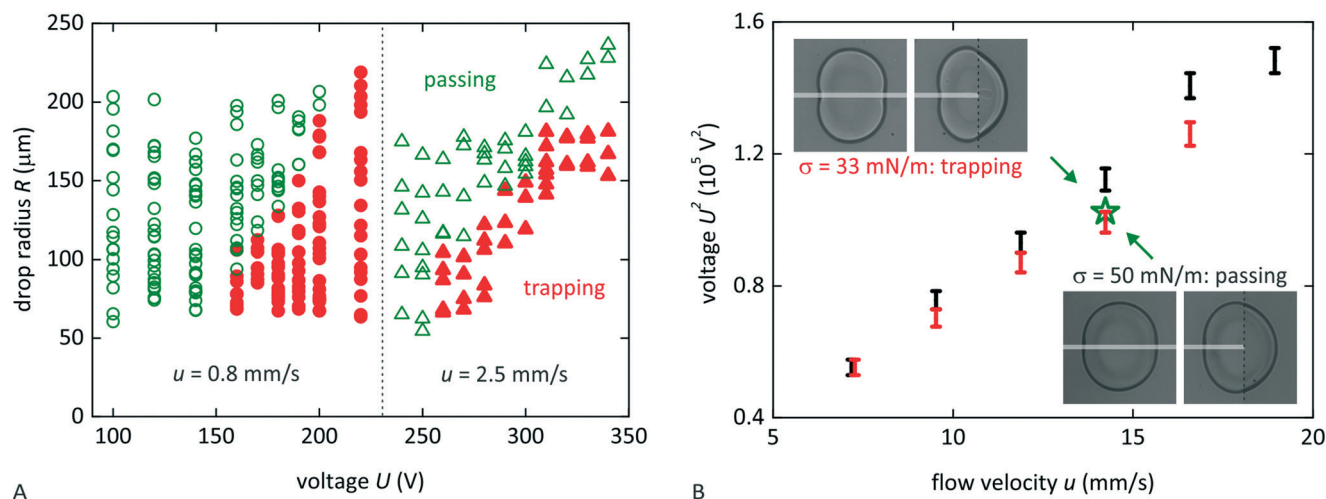

Fig. 4 Experimental trapping diagrams. (A) Depending on the applied voltage and drop radius, drops are either being trapped by (red closed symbols) or passing (green open symbols) the electrodes. Results are shown for two different velocities of the continuous phase, u = 0.8 mm s^{-1} (circles) and u = 2.5 mm s^{-1} (squares). (B) Square of the critical voltage versus the flow velocity of the continuous phase for a fixed drop size (R = 125 μm), for two different interfacial tensions, σ = 50 mN m^{-1} (black) and σ = 33 mN m^{-1} (red). The ends of the error bars indicate the minimum and maximum voltages for which we observed trapping and passing, respectively. The pictures show drops with σ = 50 mN m^{-1} (lower right, passing the electrodes) and σ = 33 mN m^{-1} (upper left, being trapped by the electrodes) at u = 14.2 mm s^{-1} and U = 320 V (as indicated by the star), just before and above the electrode edge. The gaps between the electrodes are indicated in white.
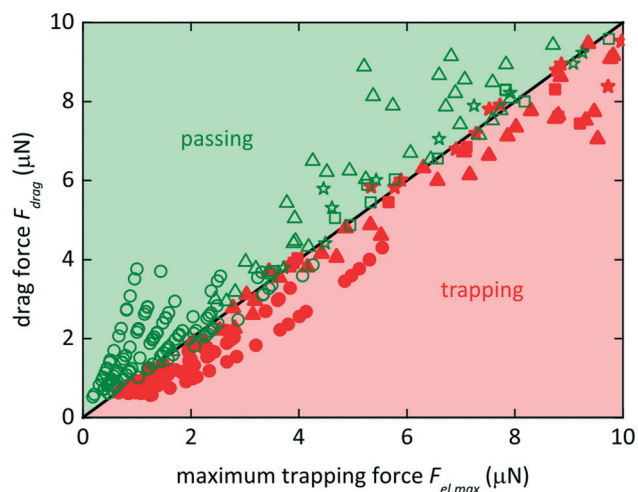
Fig. 5 Drag force *versus* maximum trapping force for the experimental results in Fig. 4A (u = 0.8 mm s^{-1} (circles), u = 2.5 mm s^{-1} (triangles); σ = 50 mN m^{-1}) and Fig. 4B (σ = 50 mN m^{-1} (squares), σ = 33 mN m^{-1} (stars); R = 125 μm). The transition from passing (green open symbols) to trapping (red closed symbols) occurs when both forces are equal.

confirming the proposed model. Quantitative deviations should actually be expected for small drops ($R \sim h$), where our assumption of a disc-like drop shape breaks down, affecting both the electrostatic trapping force as well as the drag force. Similarly, deviations from a circular shape for large drops ($R \gg h$) or small interfacial tensions (see Fig. 4B) are not taken into account in our model. Yet, as Fig. 5 shows, the consequences for the prediction of the trapping threshold are minor for the range of parameters studied here, *i.e.* in particular for electrostatic trapping forces up to 10 μN. Note that these forces are one to two orders of magnitude larger than the forces of 0.1 to 1 μN reported for geometric traps.[15] Moreover, electrostatic traps offer the additional advantage of being switchable, enabling on-demand trapping and release of drops by changing the applied voltage.

II. Applications

A. Guiding of drops. The principle that the electrostatic force will pull a drop towards the middle of a gap can also be used to direct drops. An example hereof is presented in Fig. 6. By placing the electrode gap at an angle α with respect to the flow direction, the electrostatic trapping force competes with the projection of the hydrodynamic driving force in the direction perpendicular to the gap. In terms of a simple force balance between the trapping and the driving force, this means that we can use the equations for a perpendicular gap, in which, however, the ratio between the hydrodynamic force and the maximum electrostatic force is now decreased by a factor of $\sin(\alpha)$. This allows for the guiding of drops even in strong flows, by designing a small value for α. By combining several electrodes in a branching geometry, drops can be guided laterally along various predefined tracks, depending on which electrodes are activated. Only n + 1 electrodes are needed to obtain n possible directions. The path of subsequent drops can be easily altered by switching between the electrodes, which offers increased flexibility as compared to guiding along topological rails.[14] After the drops are guided along different parallel tracks, they can be stopped using an independently operated array of electrostatic trapping wells located at the terminus of the guiding gaps. This combination of guiding and trapping is very suitable in scenarios where several drops have to be chemically treated or analysed in parallel for a certain amount of time; an example is the analysis of biomolecules in drops using local sensor surfaces (as *e.g.* in SPR[14]).

B. High-speed drop sorting. The guiding of drops as shown in the previous section has an intrinsic speed limitation. At higher flow speeds, drops are unable to follow the guide due to the drag force. To reduce the relevant component of the drag force, a smaller inclination angle is required, which results in longer tracks for reaching a certain lateral displacement. In lab-on-a-chip applications that involve sorting rather than slow analysis, for instance, selecting between empty and cell-containing drops or between fluorescently labelled and
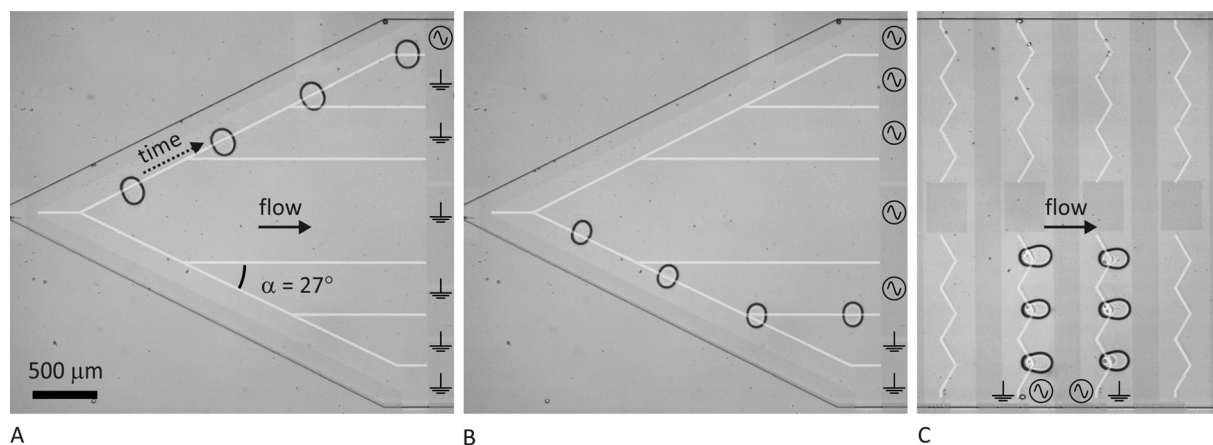

Fig. 6 Guiding and trapping of drops. (A–B) Guiding of drops along various tracks in a microchannel using a series of individually addressable electrodes. These pictures are made by combining four time frames. (C) Downstream trapping of multiple drops. The gaps between the electrodes are indicated in white.

non-labelled drops, higher handling speeds are desirable, which can be achieved by optimizing the electrode and channel design. To this end, we designed a three-electrode branching geometry underneath a Y-shaped channel (height 55 μm, width 400 μm) as shown in Fig. 7. An AC potential difference is applied continuously across the upper and lower electrodes, while the middle electrode is switched between the applied potential and ground electrode, effectively switching the path of the drop from one outlet to the other. Drops approach the Y-junction exactly in the middle of the channel and only require a small deflection to be directed to either outlet.

In this experiment, we generated water drops in mineral oil ($μ ≈ 30$ mPa s) using a flow focusing device. Depending on the flow rates of the water and oil phase, confined drops can be generated at 10 to 1000 Hz. To avoid hydrodynamic interactions, the distance between subsequent drops can be increased by increasing the oil flow rate. The maximum electrostatic force is exerted when the centre of the drop is at a distance of $\sim 0.67R$ from the gap (see section IA). The optimum design for deflecting drops that flow at a high speed (and hence experience large hydrodynamic forces) requires that the gaps are not centred below the outlet channels, but rather are offset towards the outer walls. With the gaps incorporated in this way, we observe that the drops end up approximately in the centres of the outlet channels. The applied potential is a 10 kHz sine wave at 225 V. For the middle electrode, the sine is modulated by a square waveform. When the middle electrode is at 0 V, drops are directed to the lower channel, and when it is at 255 V, drops

are directed to the upper channel. Modulating the middle electrode at half the frequency of drop generation allows alternate sorting of drops (Movie S2†). It is also possible to select a single drop from a train of drops by applying a short pulse lasting one period of drop generation (Movie S3†). In combination with a detection technique, e.g. optical or electrical,[46] our device could be used as an active sorter.

With the current device and materials used, we were able to sort 100 drops per second. At higher drop generation rates, the drag force becomes too large for the electrostatic force to pull the drop towards the desired outlet. However, the geometry of the channel and the electrodes could be optimized to achieve higher sorting rates. Since the drag scales linearly with the viscosity of the continuous phase, the drag could be reduced (and hence the sorting frequency is increased) by using oils with a lower viscosity. Another option is to decrease the inclination angle of the branching electrodes.

Electrostatic potential wells and dielectrophoresis (DEP)[31,33] both make use of electric fields for drop sorting. DEP comprises the motion of liquid drops, particles, or biological cells in a non-uniform electric field and relies on differences in the (frequency-dependent) dielectric constant with the continuous phase. Obtaining the force for the actual device geometry thus requires calculation of the electric field gradients. In addition, sorting cell-containing drops from empty drops in ambient oil involves the use of physiological strength buffers with a relatively large conductivity, i.e. typically 15 mS cm^{-1}. Manipulation using DEP requires a frequency of hundreds of MHz in this case.[47,48] In contrast, manipulation using electrostatic potential wells relies on the sharp contrast between conductive drops in an insulating medium. Our method is thus especially suitable for this application, while using lower frequencies and voltages as compared to DEP.

C. Drop deformations and splitting. The aforementioned drop deformations can be explained via minimization of the sum of the electrostatic and interfacial energies. As the drop deforms perpendicular to the gap, the total area above the electrodes increases at the cost of the area above the gap. Thus, the presence of a gap is critical to these deformations. The resulting decrease in electrostatic energy is balanced by the increase in interfacial energy associated with the increase in surface area. Minimizing the total energy then yields an equilibrium shape that is dependent on the applied voltage. This reasoning predicts larger drop deformations for wider gaps, larger drops, higher voltages, and lower interfacial tension. These trends are confirmed in the experiments. We chose narrow gap widths (i.e. 10 or 15 μm) and a high interfacial tension (i.e. no surfactants) for the purpose of limiting deformations.

Extreme drop deformations result in the splitting of drops as shown for high voltages in Fig. 8 and in the trapping diagram in Fig. S2A.† So while our simple force-based model would imply no limitations on the applied voltage and the absence of a role for the interfacial tension, it is the splitting of drops that limits the voltage that can be applied and thus the maximum electrostatic trapping force that can be exerted. In situations in which larger trapping forces are required or drops are
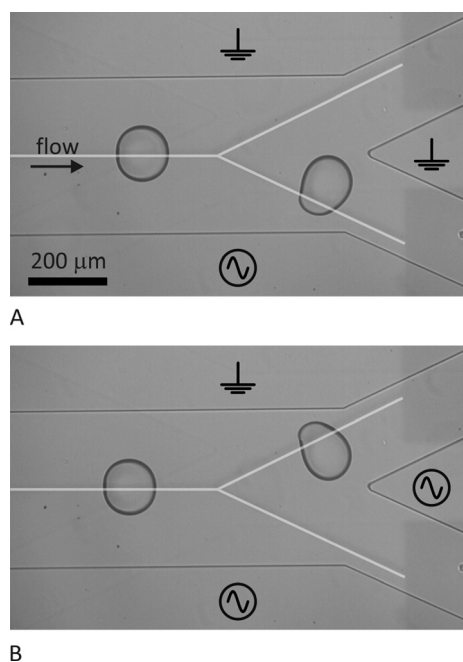

Fig. 7 Top view of a three-electrode high speed sorting geometry below a Y-shaped channel. Drops are continuously generated using a flow focusing device. By switching the middle electrode (A) on and (B) off, a drop can be forced towards either outlet. The angle of the gaps and Y-junction with respect to the inlet channel is 25°. The gaps between the electrodes are indicated in white.
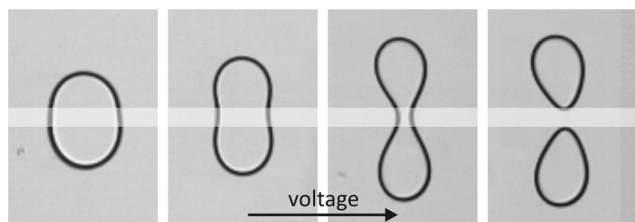
Fig. 8 Splitting of drops at high voltage and large gap width. The gap between the electrodes is indicated in white.

sensitive to break-up (*e.g.* when surfactants are used that lower the interfacial tension), the use of electrodes in a parallel plate set-up could be considered. Here, the actuation electrodes are patterned on one substrate, while the ground electrode is on the other, which eliminates the presence of a gap. This approach can be used for both trapping and guiding of drops in channels. Although a restriction in the possibilities for drop trapping, the drop splitting itself offers another interesting drop manipulation in microchannels due to its symmetry. The original drop centres above the electrode gap due to energy minimization, and thus always splits into two equally-sized drops.

Conclusions

We presented a hybrid concept for channel-based microfluidics with integrated electrowetting functionality to achieve individual control over nanoliter aqueous drops at high throughput. The trapping of drops using a co-planar electrode configuration is successfully predicted using a simple model that balances the maximum electrostatic force exerted by the trap with the hydrodynamic drag force exerted by the surrounding flow. Compared to small geometric defects, the maximum forces are an order of magnitude larger and tunable. In addition, we showed guiding and high-speed sorting of drops. We anticipate that this hybrid technology platform will enable further flexible devices combining high throughput and individual drop control.

Acknowledgements

Notes and references

1 H. Song, D. L. Chen and R. F. Ismagilov, *Angew. Chem., Int. Ed.*, 2006, **45**, 7336–7356.

2 M. T. Guo, A. Rotem, J. A. Heyman and D. A. Weitz, *Lab Chip*, 2012, **12**, 2146–2155.

3 P. Garstecki, M. J. Fuerstman, H. A. Stone and G. M. Whitesides, *Lab Chip*, 2006, **6**, 437–446.

4 T. Thorsen, R. W. Roberts, F. H. Arnold and S. R. Quake, *Phys. Rev. Lett.*, 2001, **86**, 4163–4166.

5 S. L. Anna, N. Bontoux and H. A. Stone, *Appl. Phys. Lett.*, 2003, **82**, 364–366.

6 S. Sugiura, M. Nakajima, S. Iwamoto and M. Seki, *Langmuir*, 2001, **17**, 5562–5566.

7 K. van Dijke, G. Veldhuis, K. Schroen and R. Boom, *Lab Chip*, 2009, **9**, 2824–2830.

8 K. van Dijke, R. de Ruiter, K. Schroen and R. Boom, *Soft Matter*, 2010, **6**, 321–330.

9 C. N. Baroud, F. Gallaire and R. Dangla, *Lab Chip*, 2010, **10**, 2032–2045.

10 R. Seemann, M. Brinkmann, T. Pfohl and S. Herminghaus, *Rep. Prog. Phys.*, 2012, **75**, 016601.

11 H. Gu, M. H. G. Duits and F. Mugele, *Int. J. Mol. Sci.*, 2011, **12**, 2572–2597.

12 H. Boukellal, S. Selimovic, Y. W. Jia, G. Cristobal and S. Fraden, *Lab Chip*, 2009, **9**, 331–338.

13 M. Sun, S. S. Bithi and S. A. Vanapalli, *Lab Chip*, 2011, **11**, 3949–3952.

14 P. Abbyad, R. Dangla, A. Alexandrou and C. N. Baroud, *Lab Chip*, 2011, **11**, 813–821.

15 R. Dangla, S. Lee and C. N. Baroud, *Phys. Rev. Lett.*, 2011, **107**, 124501.

16 Y.-C. Tan, Y. L. Ho and A. P. Lee, *Microfluid. Nanofluid.*, 2007, **3**, 495–499.

17 X. Niu, S. Gulati, J. B. Edel and A. J. deMello, *Lab Chip*, 2008, **8**, 1837–1841.

18 D. R. Link, S. L. Anna, D. A. Weitz and H. A. Stone, *Phys. Rev. Lett.*, 2004, **92**, 054503.

19 L. Salkin, A. Schmit, L. Courbin and P. Panizza, *Lab Chip*, 2013, **13**, 3022–3032.

20 S. Protiere, M. Z. Bazant, D. A. Weitz and H. A. Stone, *EPL*, 2010, **92**, 54002.

21 E. Fradet, C. McDougall, P. Abbyad, R. Dangla, D. McGloin and C. N. Baroud, *Lab Chip*, 2011, **11**, 4228–4234.

22 W. Wang, C. Yang, Y. S. Liu and C. M. Li, *Lab Chip*, 2010, **10**, 559–562.

23 F. Mugele and J. C. Baret, *J. Phys.: Condens. Matter*, 2005, **17**, R705–R774.

24 R. B. Fair, *Microfluid. Nanofluid.*, 2007, **3**, 245–281.

25 M. G. Pollack, R. B. Fair and A. D. Shenderov, *Appl. Phys. Lett.*, 2000, **77**, 1725–1726.

26 S. K. Cho, H. J. Moon and C. J. Kim, *J. Microelectromech. Syst.*, 2003, **12**, 70–80.

27 M. J. Jebrail, M. S. Bartsch and K. D. Patel, *Lab Chip*, 2012, **12**, 2452–2463.

28 M. Zagnoni and J. M. Cooper, *Lab Chip*, 2009, **9**, 2652–2658.

29 C. Priest, S. Herminghaus and R. Seemann, *Appl. Phys. Lett.*, 2006, **89**, 134101.

30 M. Abdelgawad, M. W. L. Watson and A. R. Wheeler, *Lab Chip*, 2009, **9**, 1046–1051.

31 K. Ahn, C. Kerbage, T. P. Hunt, R. M. Westervelt, D. R. Link and D. A. Weitz, *Appl. Phys. Lett.*, 2006, **88**, 024104.

32 W. Wang, C. Yang and C. M. Li, *Lab Chip*, 2009, **9**, 1504–1506.

33 J. C. Baret, O. J. Miller, V. Taly, M. Ryckelynck, A. El-Harrak, L. Frenz, C. Rick, M. L. Samuels, J. B. Hutchison, J. J. Agresti, D. R. Link, D. A. Weitz and A. D. Griffiths, *Lab Chip*, 2009, **9**, 1850–1858.

34 F. Malloggi, S. A. Vanapalli, H. Gu, D. van den Ende and F. Mugele, *J. Phys.: Condens. Matter*, 2007, **19**, 462101.

35 H. Gu, F. Malloggi, S. A. Vanapalli and F. Mugele, *Appl. Phys. Lett.*, 2008, **93**, 183507.

36 U. C. Yi and C. J. Kim, *J. Micromech. Microeng.*, 2006, **16**, 2053–2059.

37 L. Malic, T. Veres and M. Tabrizian, *Biosens. Bioelectron.*, 2011, **26**, 2053–2059.

38 D. J. C. M. 't Mannetje, A. G. Banpurkar, H. Koppelman, M. H. G. Duits, D. van den Ende and F. Mugele, *Langmuir*, 2013, **29**, 9944–9949.

39 T. Franke, A. R. Abate, D. A. Weitz and A. Wixforth, *Lab Chip*, 2009, **9**, 2625–2627.

40 D. C. Duffy, J. C. McDonald, O. J. A. Schueller and G. M. Whitesides, *Anal. Chem.*, 1998, **70**, 4974–4984.

41 H. S. Hele-Shaw, *Trans. R. Inst. Nav. Archit.*, 1898, **40**.

42 T. B. Jones, K. L. Wang and D. J. Yao, *Langmuir*, 2004, **20**, 2813–2818.

43 A. Staicu and F. Mugele, *Phys. Rev. Lett.*, 2006, **97**, 167801.

44 J. S. Lee and Y. C. Fung, *J. Fluid Mech.*, 1969, **37**, 657–670.

45 S. A. Vanapalli, A. G. Banpurkar, D. van den Ende, M. H. G. Duits and F. Mugele, *Lab Chip*, 2009, **9**, 982–990.

46 E. W. M. Kemna, L. I. Segerink, F. Wolbers, I. Vermes and A. van den Berg, *Analyst*, 2013, **138**, 4585–4592.

47 T. B. Jones, J. D. Fowler, Y. S. Chang and C. J. Kim, *Langmuir*, 2003, **19**, 7646–7651.

48 R. Pethig, *Biomicrofluidics*, 2010, **4**, 022811.